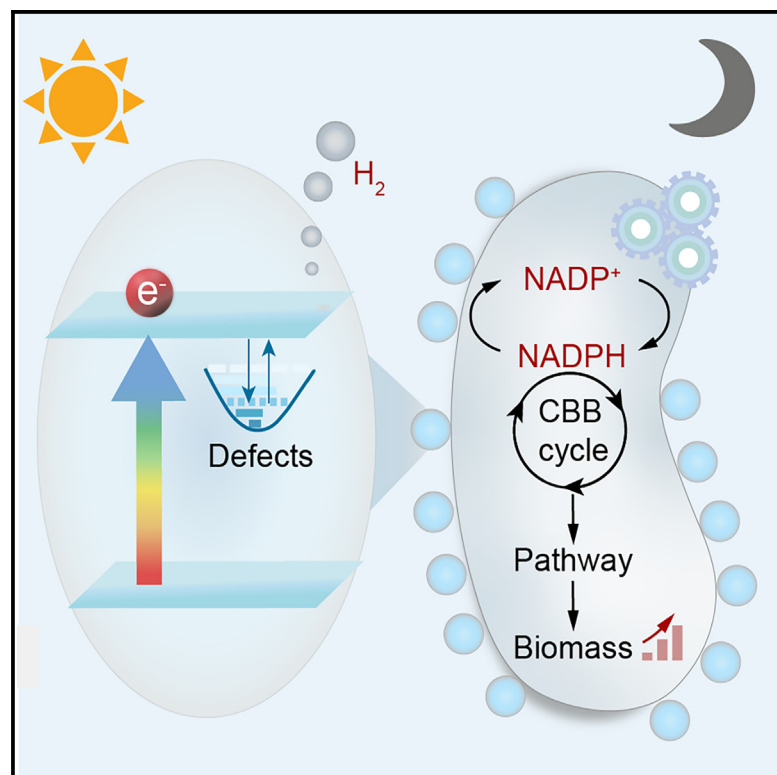


Beyond natural synthesis via solar-decoupled biohybrid photosynthetic system

Graphical abstract



Highlights

- A solar-decoupled biohybrid strategy allows for beyond-natural synthesis
- Defect engineering was proposed for higher solar energy storage efficiency
- A persistent catalyst equips photoautotrophic microbes for all-weather biomanufacturing
- The biohybrid strategy might be applicable in space, where solar energy is limited

Authors

Na Chen, Jing Xi, Tianpei He, ..., Tianyou Peng, Tiangang Liu, Quan Yuan

Correspondence

lileiyu@whu.edu.cn (L.Y.), zhangy@fjirsm.ac.cn (Y.Z.), yuanquan@whu.edu.cn (Q.Y.)

In brief

The proposed solar-decoupled biohybrid strategy, by integrating a persistent photocatalyst with photosynthetic microbes, enables the decoupling of light and dark reactions, thus realizing all-weather CO₂ utilization and long-chain chemical biosynthesis. With the development of synthetic biology, the strategy proposed in this work might provide a universal platform for the photosynthetic microorganism to “work harder day and night” to achieve higher yields and offer new ideas for sustainable energy storage and utilization.



Chen et al., 2025, Chem 11, 102381
April 10, 2025 © 2024 Elsevier Inc. All rights are reserved, including those for text and data mining, AI training, and similar technologies.
<https://doi.org/10.1016/j.chempr.2024.11.019>

Article

Beyond natural synthesis via solar-decoupled biohybrid photosynthetic system

Na Chen,^{1,5} Jing Xi,^{1,5} Tianpei He,^{1,5} Ruichen Shen,² Rui Zhao,¹ Haoming Chi,¹ Jia Yao,¹ Na Du,¹ Lilei Yu,^{1,*} Yun Zhang,^{4,*} Tianyou Peng,¹ Tiangang Liu,³ and Quan Yuan^{1,2,6,*}

¹Renmin Hospital of Wuhan University, College of Chemistry and Molecular Sciences, Institute of Molecular Medicine, School of Microelectronics, School of Pharmaceutical Sciences, Wuhan University, Wuhan 430072, P.R. China

²Molecular Science and Biomedicine Laboratory (MBL), State Key Laboratory of Chemo/Biosensing and Chemometrics, College of Chemistry and Chemical Engineering, Hunan University, Changsha 410082, P.R. China

³State Key Laboratory of Microbial Metabolism, Department of Bioengineering, School of Life Sciences and Biotechnology, Shanghai Jiao Tong University, Shanghai 200240, P.R. China

⁴State Key Laboratory of Structural Chemistry, Fujian Institute of Research on the Structure of Matter, Chinese Academy of Sciences, Fuzhou 350002, P.R. China

⁵These authors contributed equally

⁶Lead contact

*Correspondence: lileiyu@whu.edu.cn (L.Y.), zhangyf@fjirm.ac.cn (Y.Z.), yuanquan@whu.edu.cn (Q.Y.)

<https://doi.org/10.1016/j.chempr.2024.11.019>

THE BIGGER PICTURE Photosynthetic microorganisms enable the direct CO₂ conversion into highly value-added long-chain chemicals by transforming solar energy into chemical energy, offering a promising route for coupling CO₂ sequestration with sustainable development. However, the stored chemical energy, such as the critical reducing power NADPH produced in photoreactions, aims to support the microbial survival in the dark rather than biosynthesis, which inevitably sets significant limitations on practical applications. Our proposed spatiotemporal solar-decoupled biohybrid strategy in this work enables photosynthetic microorganisms to extend the photosynthetic reaction into dark conditions. This research serves as a proof of concept that could guide future studies on expanding photocatalytic reactions independent of *in situ* irradiation. It may also forge new pathways for the sustainable use of solar energy and biomanufacturing initiatives in spaces where sunlight is scarce.

SUMMARY

Inspired by the solar energy storage process during photosynthesis, we report herein a solar-decoupled photosynthetic biohybrid strategy through integrating a persistent photocatalyst with photoautotrophic microbes for sustainable and all-weather biomanufacturing, allowing for overcoming the intrinsic intermittent nature of solar energy availability by introducing energy storage and release processes. The results demonstrate that the apparent photo conversion efficiency (APCE) for of the persistent catalyst/*R. palustris* hybrid system reaches 8.30%, much higher than the 4.36% observed in bare *R. palustris*. Additionally, the proposed solar-decoupled biohybrid strategy not only shows considerable potential in coupling the practical power plant for the capture and utilization of CO₂ from the flue gas but also exhibits universal applicability in different photosynthetic microorganisms. This concept-proving research offers new ideas to extend photocatalysis reactions without *in situ* irradiation and could pave new ways for sustainable solar energy utilization as well as biomanufacturing in space, where solar energy might be limited.

INTRODUCTION

Inexhaustible solar energy is by far the largest renewable power source and has been widely regarded as one of the most attractive avenues for reducing CO₂ emission by relieving the heavy dependence on fossil fuels.^{1–5} Photosynthetic microorganism, enabling direct CO₂ conversion into highly value-

added long-chain chemicals by utilizing solar energy, offers a promising route for coupling CO₂ sequestration with sustainable development.^{6–8} Currently, the conversion of solar-to-chemical energy by photosynthetic microorganisms has drawn increasing attention owing to their great potential in simply utilizing inexhaustible sunlight and environmentally harmful CO₂ as energy and carbon sources, respectively.^{9–12} In nature,

limited by intermittent solar energy availability, photosynthetic microorganisms have evolved to decouple light and dark reactions for delayed, on-demand solar utilization, converting and storing solar energy as chemical energy.^{1,13,14} However, the stored chemical energy, such as the critical reducing power reduced nicotinamide adenine dinucleotide phosphate (NADPH) produced in photoreactions, aims to support the microbial survival in the dark rather than biosynthesis. To this end, the stored chemical energy is not nearly enough to drive the production of value-added long-chain chemicals, which inevitably sets significant limitations on the practical application.^{15–17} It is of great significance to construct a stored “energy pool” with high capacity to drive the dark reactions for all-weather and efficient CO₂ fixation and chemical biosynthesis in photosynthetic microorganisms.

Persistent photocatalysis, capable of collecting and storing photogenerated charges during periods of sunlight followed by a prolonged discharge during low-illumination periods, is expected to be an elegant solution to store solar energy.^{13,18,19} With the compatibility of photocatalysis and energy storage, persistent photocatalysis is recognized to be more compact than photovoltaic/battery systems and has attracted tremendous attention as a promising alternative for all-weather photocatalytic reactions.¹³ The construction of a spatiotemporal solar-decoupled photosynthetic biohybrid system, by integrating persistent photocatalysis with photosynthetic microorganisms, holds promise for paving new ways to overcome the intermittent characteristics of solar energy and facilitate industrial production in biomanufacturing.^{20–23} Improving the capacity of the stored energy “pool” in persistent photocatalysis and effectively coupling it with photosynthetic microorganisms for a continuous energy supply are key to achieving all-weather, efficient CO₂ fixation and biosynthesis.

Inspired by the energy storage process in the light reaction, we report herein a solar-decoupled biohybrid strategy that integrates a persistent photocatalyst with photosynthetic microbes to decouple the light and dark reactions, thus realizing all-weather, sustainable CO₂ utilization and long-chain chemical biosynthesis. Specifically, solar energy can be efficiently converted and stored as reducing hydrogen and photogenerated electrons through band engineering and defect regulation with a heteroatomic doping strategy. Subsequently, the stored reducing energy can then be released in the dark, offering a continuous driving force for the critical NADPH regeneration in photosynthetic microorganisms through microbial electron transfer-related proteins and hydrogenases. Additionally, it is worth mentioning that the proposed solar-decoupled biohybrid strategy not only shows considerable potential in coupling the practical power plant for the capture and utilization of CO₂ from the flue gas but also exhibits universal applicability in different photosynthetic microorganisms. As Nobel Prize winner Wilhelm Ostwald said, “[T]he history of civilization becomes the history of man’s advancing control over energy” in “The modern theory of energetics,”²⁴ we believe that the proposed energy control strategy and the solar-decoupled biohybrid concept offer new ideas for advancing social civilization development.

RESULTS AND DISCUSSION

Rational design of the spatiotemporally solar-decoupled biohybrid

Persistent photocatalysis, capable of collecting and storing photogenerated charges, is recognized as an elegant solution to cloud intermittency and the evening demand issue.¹³ Integrating the battery-like persistent photocatalysis with photosynthetic microorganism holds promise in decoupling solar utilization spatiotemporally and thus supplying energy to drive photosynthetic microorganism metabolism in the dark. NADPH, an essential cofactor in redox reactions, is pivotal in microbial biosynthesis pathways.¹⁵ Previous studies have demonstrated that the reducing H₂ or electrons were capable of driving the regeneration of the critical reducing power NADPH in microorganisms.^{7,15,25} Constructing a biohybrid in which a persistent photocatalyst enables converting solar energy into the reducing H₂ or electrons is promising to supply a driving force for the continuous regeneration of NADPH, without causing metabolic imbalance, thus achieving efficient anabolism in both light and dark conditions.

Herein, as a proof of concept, a solar-decoupled biohybrid was developed by integrating the persistent photocatalysis of Zn_{1.2}Ga_{1.6}Ge_{0.2}O₄ (ZGGO) with the photosynthetic microorganism of *Rhodospseudomonas palustris* (*R. palustris*) for this study. Specifically, as illustrated in Figure 1, solar energy can be converted into chemical energy in H₂ through the hydrogen evolution reaction (HER), while photoinduced electrons can be stored in defects. Particularly worth mentioning is that defect engineering, capable of tuning the electronic structures for enriched energy storage sites, can be adopted to expand the capacity of stored energy.^{25–27} Subsequently, the stored reducing energy, including H₂ and photoelectrons derived from the persistent photocatalyst, can act as reducing agents to supply the critical reducing power NADPH through H₂ delivery and charge transfer to the photosynthetic microorganism in the dark, overcoming the limitation of NADPH level in the dark and thus achieving all-weather and efficient biosynthesis. Overall, by integrating persistent photocatalysis and photosynthetic microorganism, a spatiotemporally solar-decoupled photosynthetic biohybrid system was then constructed.

Defect engineering for higher solar energy storage efficiency

Structural defects can function as electron traps, which are capable of capturing and storing a large number of electrons triggered by solar irradiation.^{15,28} In addition, defects allow for band-gap optimization and efficient charge separation.²⁹ Heteroatomic doping strategy has been widely adopted in defect regulation and charge storage.^{25,30,31} As shown in Figure 2A, it can be clearly seen that, by heteroatomic doping with Ni ions, the average H₂ evolution rate increased by about 4.97 times (Figure S1), which is comparable to the ones reported in previous literature (Table S1). To understand the promoted H₂ evolution rate of Ni-doped persistent catalyst, density functional theory (DFT) calculations were further performed. As shown in Figure S2, the adsorption energies of H atoms on ZGGO and ZGGO:Ni were calculated to be 138.15 and 42.19 kJ/mol,

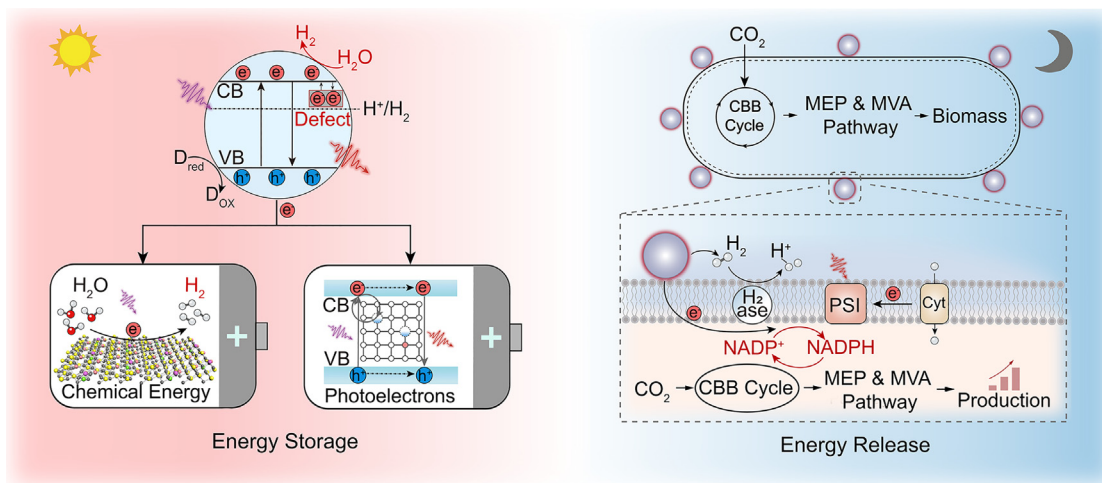


Figure 1. Schematic illustration of the spatiotemporally solar-decoupled biohybrid

Persistent photocatalysis drives the all-weather generation of the critical reducing power NADPH by converting and storing solar energy into the reducing driving forces of H₂ and photoelectrons, thus achieving highly efficient and sustainable CO₂ fixation and biosynthesis in photosynthetic microbes.

respectively, indicating that ZGGO:Ni is more favorable for adsorbing H atoms. It can be deduced that the higher catalytic activity of ZGGO:Ni can be partially attributed to the enrichment and concentration of H atoms in the local environment. The 2D differential charge density diagrams in Figure S3 demonstrate that the charge density around Ni decreases, suggesting a very local influence on the host material (Tables S2 and S3). Moreover, according to the DFT calculations, the band structure and density of states (DOS) shown in Figures 2B and 2C demonstrate that Ni doping narrows the band gap. Based on the UV-vis diffuse reflectance spectra and ultraviolet photoelectron spectroscopy (UPS) measurements shown in Figures S4 and S5, the band gaps of ZGGO and ZGGO:Ni are calculated to be 4.28 and 4.17 eV, respectively. Consistent with the DFT calculations, these results indicate that the Ni doping strategy narrows the band gap (Figure 2D). Overall, we rationalize that the Ni ion doping strategy regulates the electronic structure and narrows the band gap of the persistent photocatalysis, which partially contributes to the improved H₂ evolution rate. Additionally, the low-temperature electron paramagnetic resonance (EPR) spectra in Figure 2E clearly show two paramagnetic centers in both ZGGO and ZGGO:Ni. According to previous reports,^{32,33} g-factors at 2.00 and 2.02 can be assigned to electrons trapped in oxygen vacancy (V_O) and holes delocalized on oxygen atoms around V_{G_e}, respectively. It can be observed that the EPR intensity of both the V_O and V_{G_e} increased in the ZGGO:Ni samples, demonstrating that the Ni ion doping strategy is effective for regulating the defect structure to enrich energy storage sites (Figures S6 and S7).

The photocurrent curves in Figure 2F demonstrate that both the persistent photocatalysis of ZGGO and ZGGO:Ni experienced very slow photocurrent decay with irradiation off, suggesting that the persistent photocatalyst can store photoelectrons and release them slowly in the dark.³⁴ By stimulating a short-cycle intermittent irradiation condition in nature, it was found that the persistent photocatalysis of ZGGO:Ni evolved

1.50 mmol h⁻¹ g⁻¹ hydrogen on average, which is more efficient than continuous irradiation for 1.5 h (blue line: hydrogen yield of 1.38 mmol h⁻¹ g⁻¹) (Figure 2G). The result further validates that the persistent photocatalysis of ZGGO:Ni can store photoelectrons for continuous HER in the dark. In addition, the persistent photocatalysis of ZGGO:Ni shows persistent luminescence (PL) even after the irradiation ceases (Figures 2H and S8), which can be ascribed to the trapped electron-hole recombination.^{35–38} To explore the photoelectron accumulation process, photoinduced vacancies in ZGGO:Ni were further investigated. As shown in Figure S9, an intensive EPR signal (g = 2.00), which can be assigned to electrons trapped in V_O, can be clearly observed. In addition, the EPR signal intensity increased upon illumination, suggesting more electron injection and accumulation in V_O (Figures S10 and S11). Furthermore, the energy storage stability of the persistent catalyst was also evaluated. As shown in Figure S12, both the H₂ evolution rate and the PL intensity were largely sustained. Collectively, the above results confirm that the persistent photocatalysis with high stability is capable of transforming and storing solar energy in the daytime and then releasing it in the dark (Figure 2I).

Solar-decoupled biohybrids driving all-weather regeneration of NADPH

The stored energy pool derived from the persistent photocatalyst includes the transformed chemical energy of the electron carrier H₂ and the photoelectrons trapped in defect structures. To test whether the stored energy can drive NADPH regeneration in the dark, β-nicotinamide-adenine dinucleotide phosphate (NADP⁺) reduction tests were first performed *in vitro*. Figure 3A shows an obvious absorbance peak of NADPH around 340 nm in the lysate from photosynthetic microorganisms *R. palustris* upon the injection of the reducing agent H₂ in the dark, while no peak is observed in the bare lysate, which can be ascribed to the reducing power delivered by the microbial hydrogenases.^{39–42} Figure 3B shows that the NADPH regeneration ratio

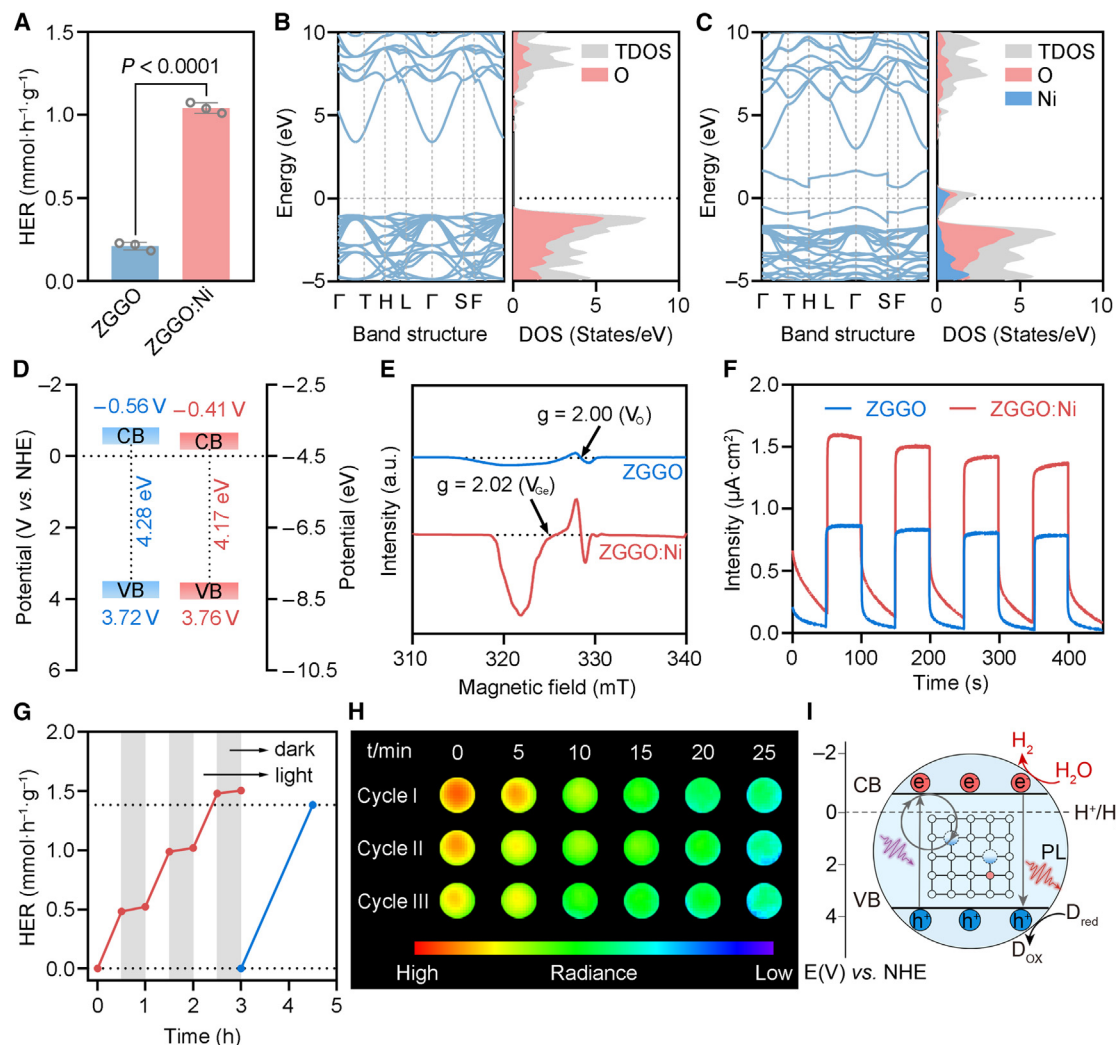


Figure 2. Heteroatomic Ni doping strategy for defect and electronic structure regulation

(A) H₂ evolution rate of the persistent photocatalyst. Data are presented as mean values \pm SD, $n = 3$. Statistical significance (represented by p value) was calculated via two-tail Student's t test.

(B and C) Band structure and DOS of the persistent photocatalyst: (B) ZGGO and (C) ZGGO:Ni predicted using the HSE06 functional.

(D) Energy level diagram of the persistent photocatalyst measured by UPS and inverse photoelectron spectroscopy (IPES).

(E) EPR spectra of the persistent photocatalyst.

(F) Photocurrent responses under 300 W xenon lamp illumination.

(G) H₂ evolution rate of the persistent photocatalyst ZGGO:Ni loaded with 3 wt % Pt under intermittent or continuous illumination.

(H) Persistent luminescence decay images of the persistent photocatalyst ZGGO:Ni.

(I) Schematic illustration of the energy storage processes in the persistent photocatalyst.

increased gradually during the light-dark cycle upon the addition of the persistent photocatalyst ZGGO:Ni, with the final value reaching 36.30%, which is higher than the one under continuous irradiation for 2 h. The above results validate that both the stored energy of H₂ and photoelectrons derived from the persistent catalyst drive the critical reducing power NADPH regeneration process in the dark (Figure 3C).

Subsequently, the influence of the persistent catalyst on microbial NADPH regeneration was further investigated *in vivo*. Considering that direct interactions at the persistent photocatalyst microbe interface are beneficial for the delivery of the electron

carrier H₂ and the electron transfer process,^{43–45} the physical interface interactions and compatibility between the persistent photocatalyst and *R. palustris* were explored (Figures S13–S15). Scanning electron microscope (SEM) mapping in Figure S16 demonstrates that the persistent photocatalyst is in close contact with the microorganism, suggesting effective interface self-assembly. The self-assembly between the persistent photocatalyst and *R. palustris* is presumably owing to van der Waals interactions through the opposite electrostatic potentials (Figure S17). According to the Langmuir-type adsorption model, the average number of persistent photocatalyst nanoparticles per microbe

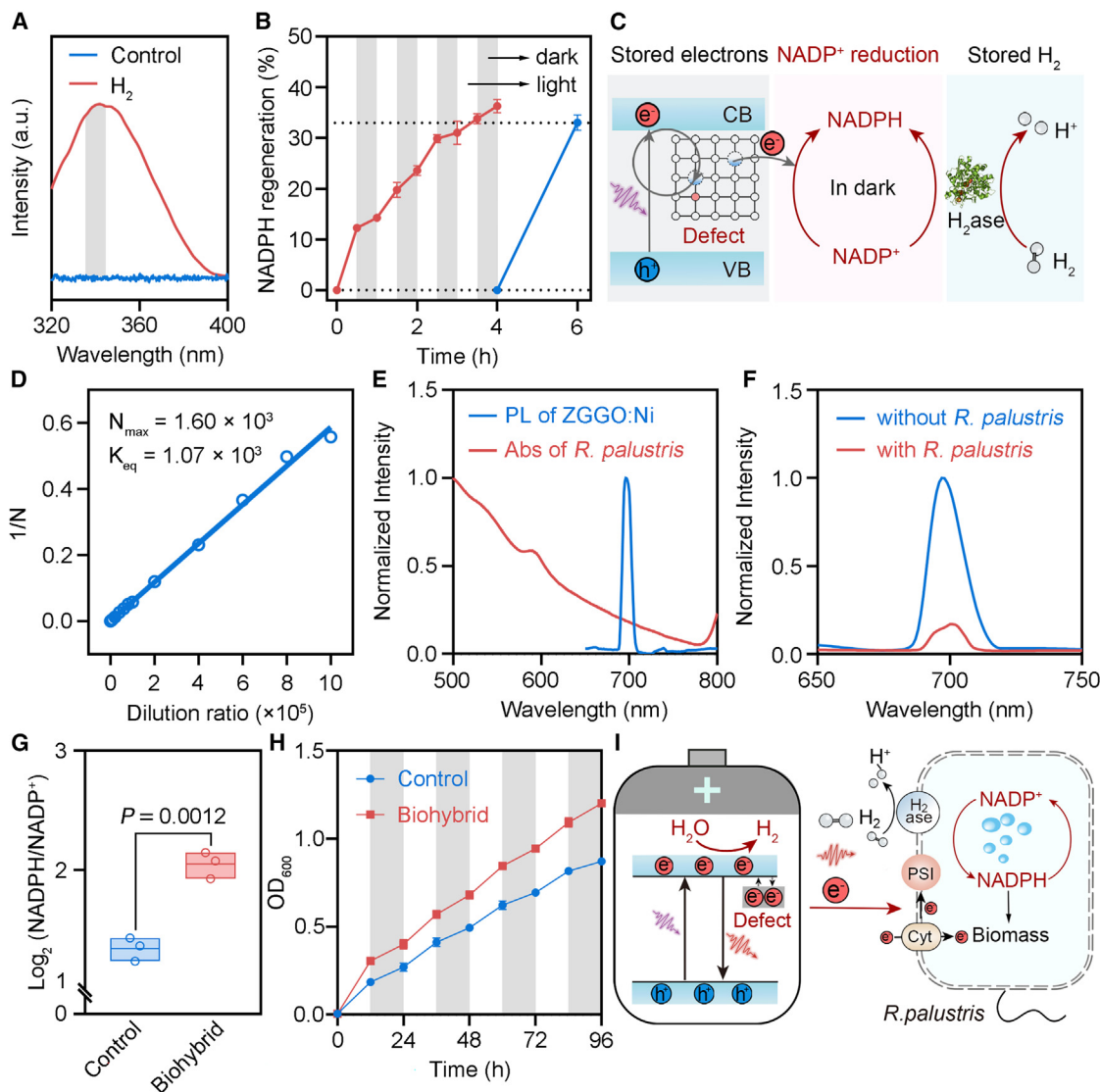


Figure 3. The stored energy pool derived from the persistent catalyst drives NADPH regeneration in the dark

- (A) NADPH regeneration ratio upon the injection of H_2 in the lysate from *R. palustris*.
 (B) NADPH regeneration ratio across time under intermittent and continuous illumination. Data are presented as mean values \pm SD, $n = 3$.
 (C) Schematic illustration of the stored energy for NADPH generation *in vitro*.
 (D) Plot of $1/N$ vs. the dilution ratio of the persistent catalyst ZGGO:Ni.
 (E) Normalized UV-vis absorption spectra of *R. palustris*. Persistent luminescence spectra of the persistent catalyst ZGGO:Ni ($\lambda_{ex} = 290$ nm).
 (F) Persistent luminescence of bare persistent catalyst ZGGO:Ni and the persistent catalyst/*R. palustris*.
 (G) $\text{Log}_2(\text{NADPH}/\text{NADP}^+)$ in *R. palustris*. Data are presented as mean values \pm SD, $n = 3$. Box edges indicate the upper and lower quartiles, the centerlines indicate the mean value, and the horizontal bars indicate the maximum and minimum values. Statistical significance (represented by p value) was calculated via two-tail Student's t test.
 (H) OD_{600} of *R. palustris* across time under intermittent or continuous illumination in shake-flask fermentation.
 (I) Schematic illustration of solar-decoupled biohybrids driving the regeneration of NADPH in the dark.

(N) was quantitatively determined.⁴² As shown in Figure 3D, it can be observed that the dilution ratio of nanoparticles has a linear relationship with $1/N$. Consequently, the dimensionless equilibrium constant K_{eq} and the maximum number of adsorbed nanoparticles per bacterial cell were calculated to be 1.07×10^3 and 1.60×10^3 , respectively (Figure S18).⁴²

To elucidate the stored charge transfer process between the persistent photocatalyst and the microbe, the PL emission spectra were further measured. Figure 3E shows that the PL emission peaking at 696 nm overlaps with the absorption spectra of *R. palustris* and pigment molecules,⁴¹ and Figure 3F further shows that the addition of *R. palustris* or pigment molecules totally

quenches the emission (Figures S19 and S20), indicating that the stored photoelectrons could be transferred to *R. palustris* or pigment molecules instead of recombination luminescence (Figure S21). Specifically, according to the formulas in the methods section and the calculated lifetime of photoexcited states in Figure S22, the rate constant of charge transfer between the catalyst and microbes (k_{ET}) was calculated to be $1.22 \times 10^6 \text{ s}^{-1}$, which is much larger than the total value of non-radiative recombination (k_{NR}) and radiative electron-hole recombination (k_{PL}) ($k_{NR} + k_{PL} = 1.93 \times 10^5 \text{ s}^{-1}$), further validating the rapid transfer of electrons to the microbes.⁴² The above results demonstrate that the persistent catalyst could enhance photosynthetic efficiency of photosystem I (PSI) (responsible for light absorption, capture, utilization, and electron transfer).⁴¹

Finally, to test whether the persistent catalyst facilitates the regeneration of the critical reducing power of NADPH, the NADPH was quantitatively determined. As shown in Figure 3G, it demonstrates that the $\log_2(\text{NADPH}/\text{NADP}^+)$ value in persistent photocatalyst/*R. palustris* hybrid is higher than that in bare *R. palustris* after 4 days of culture under intermittent irradiation (Figure S23), confirming that the persistent photocatalyst can be utilized to drive the all-weather generation of the critical reducing equivalent NADPH. The increased level of NADPH/NADP⁺ ratio could be ascribed to the supply of reducing energy, including H₂ and electrons, both in light and dark. Additionally, the higher level of OD₆₀₀ in the biohybrid system (Figure 3H) further validates that the persistent photocatalyst facilitates microbial metabolism (Figure S24). Overall, the above *in vitro* and *in vivo* experimental results reveal that the constructed solar-decoupled biohybrid could drive the all-weather regeneration of NADPH through multiple ways, including H₂ delivery, charge transfer, and the enhanced photosynthetic efficiency of PSI (Figure 3I).

Persistent photocatalyst-induced regulation of microbial metabolism

As shown in Figures 4A and 4B, both the CO₂ fixation rates and the lycopene biosynthesis yields in persistent catalyst/*R. palustris* biohybrid are higher across time compared with the bare *R. palustris*, not only during the daytime but also at night. It can be seen that the CO₂ fixation rate and the lycopene biosynthesis yields in the solar-decoupled biohybrid are $3.17 \text{ mM g}^{-1} \text{ DCW}^{-1} \text{ h}^{-1}$ and 8.80 mg L^{-1} respectively, which are both higher compared with the bare *R. palustris* after 4 days of culture under intermittent illumination (Figures S25 and S26). Accordingly, the apparent photo conversion efficiency (APCE) values are calculated to be 8.30% for persistent catalyst/*R. palustris* hybrid and 4.36% for the bare *R. palustris* (Figure 4C).⁴⁶ To the best of our knowledge, the high APCE value represents superior performance compared with previous reports for solar-to-chemical conversion,⁴⁶ which could be partially owing to the efficient solar energy utilization in the dark. In short, the above results indicate that the solar-decoupled biohybrid strategy enables improvement of the efficiency of solar energy utilization and the photosynthetic microbial anabolism, including the Calvin-Benson-Bassham (CBB) cycle and the mevalonate (MVA) and methylerythritol 4-phosphate (MEP)

pathways, for highly efficient CO₂ fixation and lycopene biosynthesis.

Next, transcriptomics and metabolomics profiling were adopted to analyze the cellular energy and substance metabolism, aiming at an in-depth mechanism understanding of how the persistent photocatalyst regulates the microbial metabolism under intermittent illumination. Differentially expressed genes were evaluated according to the Log₂ fold change (Log₂ FC), which was calculated with $\{\text{Log}_2 [(\text{Gene read counts})_{(\text{Experimental})}] - \text{Log}_2 [(\text{Gene read counts})_{(\text{Control})}]\}$. As shown in Figure 4D, of the 4,462 transcripts detected and identified in *R. palustris*, 637 transcripts were significantly increased (p value < 0.05 and FC $\geq |1.5|$), indicating that the persistent photocatalyst upregulates these gene expressions in *R. palustris*. By assessing the mRNA expressions in *R. palustris*, it was found that the genes associated with electron transfer proteins, including pilus, c-type cytochromes, flagellum, H₂-uptake PtoABC, and flavin (Figure 4E), photosynthesis proteins (including RuBisCo, NAD(P)H, photophosphorylation; Figure 4F), CBB cycle (Figure 4G), and hydrogenase are highly expressed, as represented by Log₂ FPKM values (log base 2 of fragments per kb of exon model per million mapped fragments) in the biohybrid compared with bare *R. palustris* (Figures S27 and S28).^{47–49} The highly expressed genes typically represent the highly expressed proteins. Accordingly, it can be deduced that the persistent catalyst might improve the functions of electron transfer and photosynthesis-associated proteins, thus facilitating the electron transfer and photosynthesis processes. As illustrated in Figure S29, the addition of the electron transfer inhibitors carbonyl cyanide *m*-chlorophenyl hydrazone (CCCP) or rotenone is observed to diminish the lycopene biosynthesis yields of *R. palustris*. This observation indicates that impeded electron transfer processes lead to a reduction in the biosynthetic efficiency of the biohybrid system. In contrast, the supplementation with the electron transfer shuttle humic acid (HA) results in an enhancement of lycopene biosynthesis yields, suggesting that facilitated electron transfer processes can elevate the biosynthetic efficiency of the biohybrid system. These findings provide further validation for the mechanistic hypothesis, emphasizing the integral role of electron transfer processes in the interaction between the persistent catalyst and *R. palustris*. In addition, the Log₂ FC values of CBB-related proteins are demonstrated to be >0 on the whole (Figure 4H), and the FC values of proteins associated with the MVA and MEP pathways are demonstrated to be >1 (Figures 4I and S30). The results indicate that the genes encoding these proteins are highly expressed in the solar-decoupled biohybrid system by integrating the persistent catalyst, which helps to explain the observed increases in both the CO₂ fixation rate and the yields of lycopene biosynthesis. Furthermore, metabolomic analyses reveal that molecules associated with electron transfer, such as riboflavin, are significantly increased (Figures S31–S33). Overall, based on the above results, we propose the mechanism that the solar-decoupled biohybrid strategy could facilitate microbial metabolism by supplying and channeling the generated and stored photoelectrons and H₂ into microbes through electron transfer-related proteins and interfacial delivery, driving the continuous generation of the critical reducing power of NADPH in photosynthetic microorganisms, thus achieving all-weather and efficient CO₂ fixation and biosynthesis.

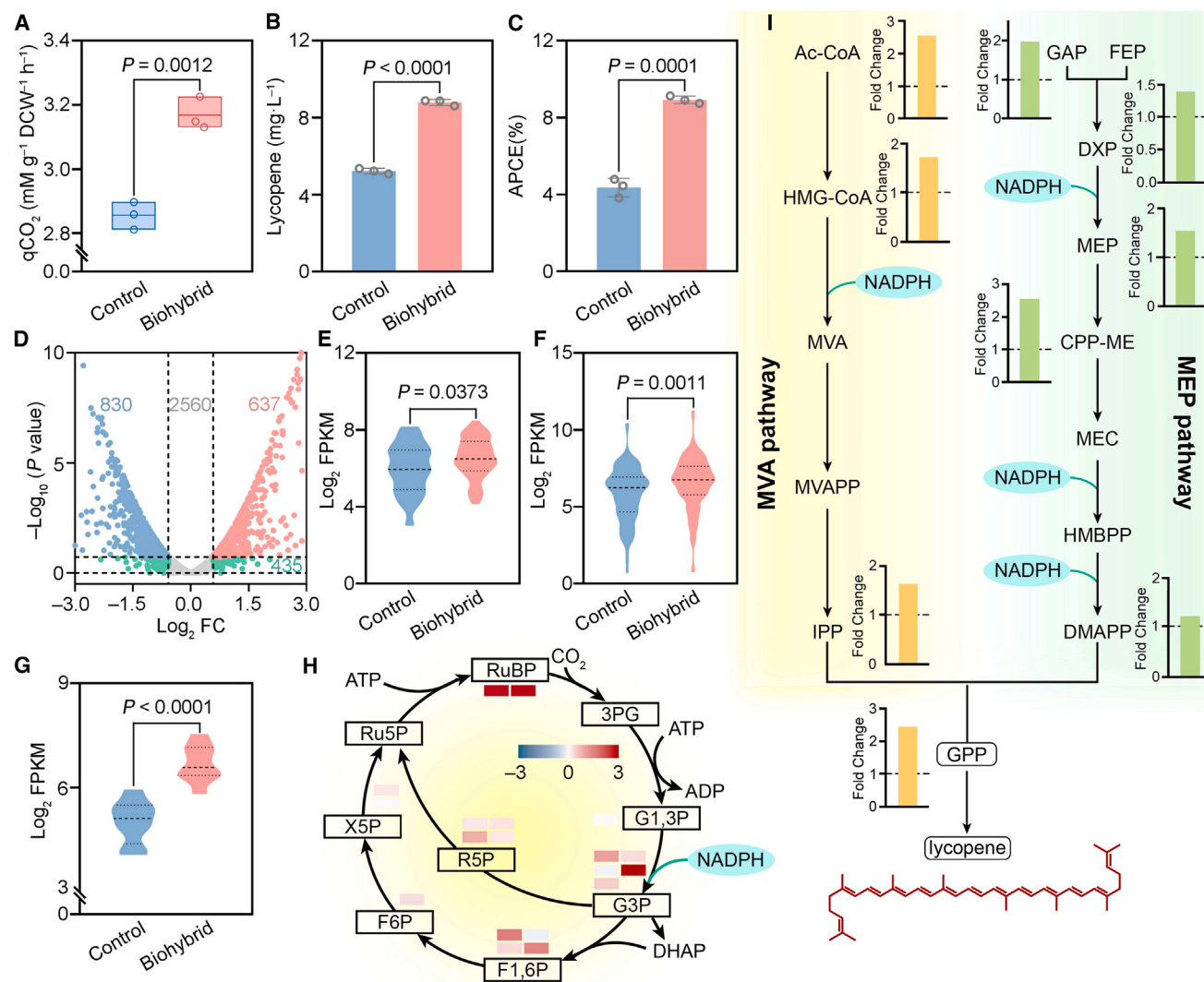


Figure 4. Molecular mechanism analysis of the persistent catalyst influence on metabolic behavior in photosynthetic microorganism *R. palustris*

(A) CO₂ fixation rate of *R. palustris* in shake-flask fermentation (DCW: dry cell weight). Data are presented as mean values ± SD, *n* = 3. Box edges indicate the upper and lower quartiles, the centerlines indicate the mean value, and the horizontal bars indicate the maximum and minimum values. Statistical significance (represented by *p* value) was calculated via two-tail Student's *t* test.

(B) Lycopene yields of *R. palustris* in shake-flask fermentation. Data are presented as mean values ± SD, *n* = 3. Statistical significance (represented by *p* value) was calculated via two-tail Student's *t* test.

(C) APCE values. Data are presented as mean values ± SD, *n* = 3. Statistical significance (represented by *p* value) was calculated via two-tail Student's *t* test.

(D) Volcano plot of differentially expressed genes in *R. palustris*. The threshold of Log₂ FC is |0.58| (i.e., FC ≥ |1.5|), and that of *p* value (calculated via two-tail Student's *t* test) is < 0.05.

(E–G) Violin plots showing significant differences in gene expression of (E) electron transfer proteins (including pilus, *c*-Cyts, flagellum, PioABC, flavin), (F) photosynthesis-related proteins (including ribulose-1,5-bisphosphate carboxylase/oxygenase (RuBisco), NAD(P)H, photophosphorylation, CBB cycle) and (G) hydrogenase in *R. palustris*. Statistical significance (represented by *p* value) was calculated via two-tail Student's *t* test.

(H and I) Differential expression analysis of genes encoding enzymes in (H) CBB cycle and (I) MVA and MEP pathways.

The practical applicability of the proposed solar-decoupled biohybrid

Practically, power plants are considered the major source of carbon dioxide emissions.^{50–52} Integrating on-site recycling technology with power plants is promising for capturing and utilizing the CO₂ emissions. To explore the potential applicability of the proposed spatiotemporally solar-decoupled photosynthetic bio-

hybrid strategy in practical use, scale-up studies on fed-batch fermentations were further performed by integrating the simulated flue gas from a coal-fired power plant. To be specific, simulated flue gas with 15 vol % CO₂ is first converted to NaHCO₃, which is then directly fed into microbial fermentation (Figure 5A).⁵³ As shown in Figure 5B, the OD₆₀₀ is higher upon the addition of the persistent photocatalyst across time under

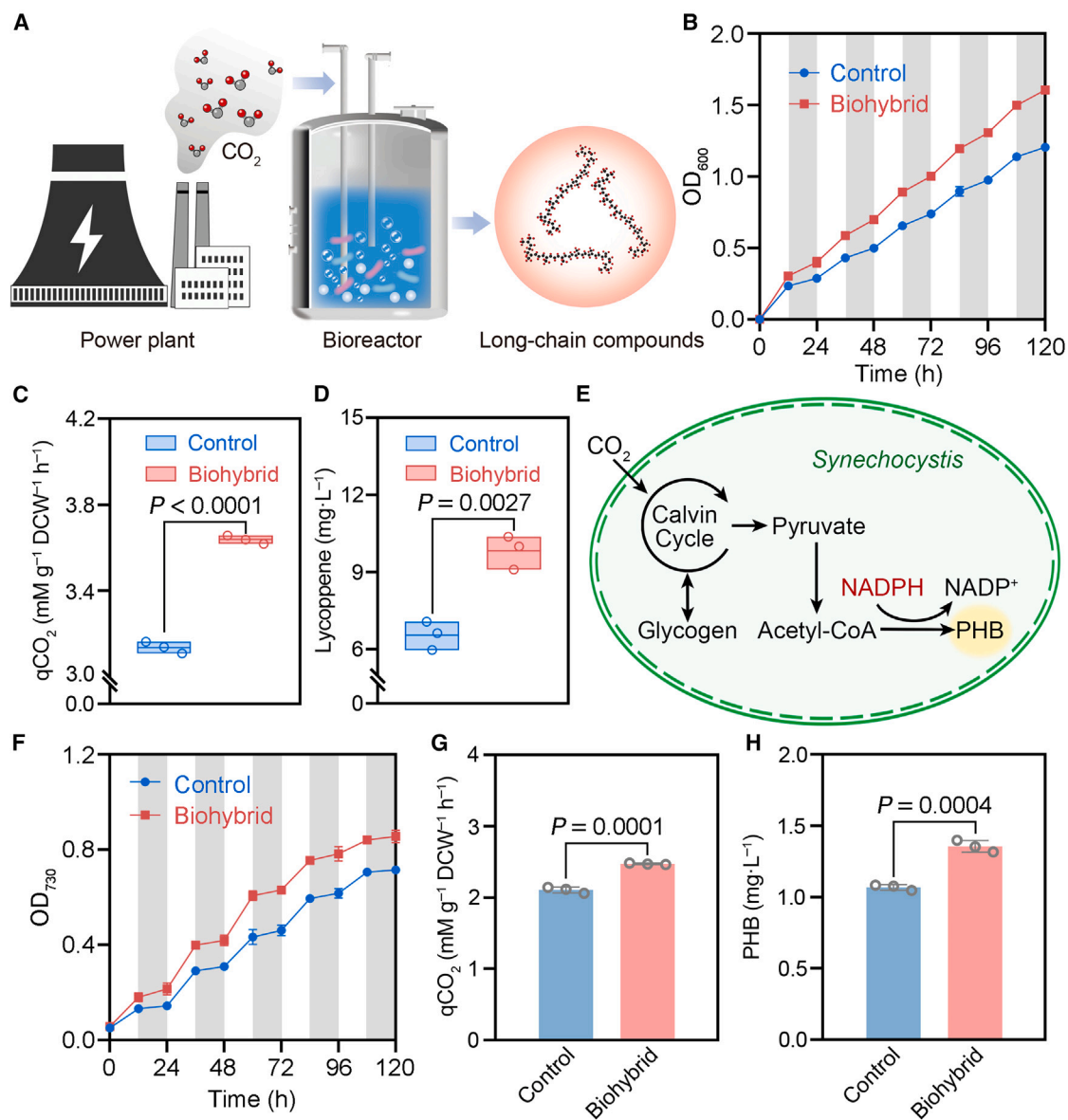


Figure 5. The practical applicability of the proposed solar-decoupled biohybrid for sustainable CO₂ fixation and long-chain chemical production

(A) Schematic illustration of the sustainable CO₂ fixation and long-chain chemical production system.

(B) The OD₆₀₀ of the *R. palustris* across fermentation time in fed-batch fermentations. Data are presented as mean values ± SD, $n = 3$. Statistical significance (represented by p value) was calculated via two-tail Student's t test.

(C) CO₂ fixation rate of *R. palustris* under the simulated intermittent illumination in fed-batch fermentations. Data are presented as mean values ± SD, $n = 3$. Box edges indicate the upper and lower quartiles, the centerlines indicate the mean value, and the horizontal bars indicate the maximum and minimum values. Statistical significance (represented by p value) was calculated via two-tail Student's t test.

(D) The lycopene biosynthesis yield of *R. palustris* under the simulated intermittent illumination in fed-batch fermentations. Data are presented as mean values ± SD, $n = 3$. Box edges indicate the upper and lower quartiles, the centerlines indicate the mean value, and the horizontal bars indicate the maximum and minimum values. Statistical significance (represented by p value) was calculated via two-tail Student's t test.

(E) Schematic illustration of the PHB metabolic pathways.

(F) The OD₇₃₀ of the *Synechocystis* across fermentation time in fed-batch fermentations. Data are presented as mean values ± SD, $n = 3$. Statistical significance (represented by p value) was calculated via two-tail Student's t test.

(G) CO₂ fixation rate of *Synechocystis* under the simulated intermittent illumination in fed-batch fermentations. Data are presented as mean values ± SD, $n = 3$. Statistical significance (represented by p value) was calculated via two-tail Student's t test.

(H) The PHB biosynthesis yield of *Synechocystis* under the simulated intermittent illumination in fed-batch fermentations. Data are presented as mean values ± SD, $n = 3$. Statistical significance (represented by p value) was calculated via two-tail Student's t test.

simulated intermittent illumination (Figure S34). Consistent with the shake-flask fermentation results, the CO₂ fixation efficiency and the lycopene biosynthesis yield in the persistent catalyst/*R. palustris* are both higher after 4 days of culture compared with bare *R. palustris* in fed-batch fermentation under simulated intermittent illumination (Figures 5C, 5D, and S35). The results validate that the proposed solar-decoupled photosynthetic biohybrid strategy is promising for coupling with practical power plants for the capture and storage of CO₂ from flue gas. Life-cycle assessment (LCA), as presented in Figure S36, further substantiates the biohybrid system's environmental and economic advantages. It shows that the biohybrid system exhibits reduced greenhouse gas (GHG) emissions, comprehensive environmental impacts, lower energy consumption, and production costs when compared to the bare *R. palustris* system. These findings underscore the biohybrid system's sustainability and efficiency in the context of ecological footprint and economic viability. Additionally, as depicted in Figure S37, the comparative CO₂ fixation rates in the biohybrid system consistently exceed those of the bare *R. palustris* system even after a duration of 24 days, which encompasses 48 light/dark cycles. This enduring performance further indicates the sustainability and robust durability of the biohybrid system.

Cyanobacteria, as promising sources of high-value-added bioactive chemicals, are able to survive in extreme environments and play key roles in atmospheric evolution as well as in synthetic biology.^{54–56} Subsequently, *cyanobacterium Synechocystis* PCC 6803 (*Synechocystis*) was further selected as a research model to explore the generalizability of the proposed solar-decoupled photosynthetic biohybrid strategy in sustainable biocatalysis and biosynthesis.^{57,58} *Synechocystis* can utilize CO₂ and produce polyhydroxybutyrate (PHB), which is recognized as an environmentally friendly bioplastic (Figure 5E). Subsequently, the universality of the proposed solar-decoupled biohybrid strategy was further explored. As shown in Figure 5F, the OD₇₃₀ of *Synechocystis* in both shake-flask and fed-batch fermentations is higher in the persistent catalyst/*Synechocystis* compared with bare *Synechocystis* under the light-dark cycle (Figure S38). Besides, both the CO₂ fixation efficiency and PHB yield are increased upon the addition of the persistent photocatalyst, as shown in Figures 5G and 5H, suggesting the applicability of the solar-decoupled biohybrid strategy in *Synechocystis* (Figures S39 and S40). Overall, the above results demonstrate the inspiring and potential application prospects of the proposed solar-decoupled photosynthetic biohybrid strategy in sustainable CO₂ utilization and green biosynthesis.

Conclusions

Our results reveal that the capacity of the stored energy derived from the persistent catalyst, including the chemical energy of the electron carrier H₂ and photoelectrons trapped in defects, can be improved through band engineering and defect engineering. Additionally, we found that the genes related to photosynthesis and electron transfer proteins were overrepresented by integrating the persistent catalyst under intermittent illumination conditions, which can be ascribed to the all-weather charge transfer and H₂ delivery to microbes. The continuous supply of reducing electrons and H₂ ultimately leads to a higher level of

NADPH and microbial metabolic activity. Furthermore, the results demonstrate that the proposed solar-decoupled biohybrid strategy has universal applicability to photosynthetic microorganisms and is promising for coupling with practical power plants for the capture and storage of CO₂ from the flue gas. Looking ahead, with the development of synthetic biology, the solar-decoupled biohybrid strategy proposed in this work might provide a universal platform for photosynthetic microorganisms to “work harder day and night” to achieve higher yields and offer new ideas for sustainable energy storage and utilization.

METHODS

Chemicals and materials

Nickel nitrate (Ni(NO₃)₂·9H₂O), zinc nitrate hexahydrate (Zn(NO₃)₂·6H₂O), gallium nitrate (Ga(NO₃)₃), sodium hydroxide (NaOH), concentrated nitric acid (HNO₃), ammonium hydroxide (NH₃·H₂O), triethanolamine (TEOA), anhydrous sodium sulfate (Na₂SO₄), anhydrous ethanol and sulfuric acid were obtained from Sinopharm Chemical Reagent (China). Germanium oxide (GeO₂), chloroplatinic acid (H₂PtCl₆), and crotonic acid were purchased from Shanghai Maclin Biochemical Technology. Chlorophyll a was purchased from Shanghai Merger Biochemical Technology. Methanol, nitrate, anhydrous acetonitrile, NaCl, n-hexane, chloroform, tetradecafluorohexane, and perfluorodecalin were purchased from Shanghai Aladdin Biochemical Technology. HA, polyformaldehyde, calcein AM, and 1-(3-chloroallyl)-3,5,7-triaza-1-azoniaadamantane chloride (PI) were purchased from Shanghai Yuan Ye Bio-Technology. Rotenone was purchased from Beijing InnoChem Science & Technology. The PBS, peptone, and beef extract were obtained from Beijing Solarbio Science & Technology. NADP⁺ and β-nicotinamide-adenine dinucleotide sodium (NAD⁺) were purchased from Shanghai BiDe Pharmaceutical Technology. NADP⁺/NADPH Assay Kit (WST-8) and Enhanced ATP Assay Kit were purchased from Beyotime Biotechnology. The bacterial strain *R. palustris* (BNCC 232041) was obtained from Bnbio., and *Synechocystis* PCC 6803 (FACHB-898) was provided by the National Aquatic Biological Resource Center.

Characterization

The hydrogen gas yield in the photocatalytic system was measured with gas chromatography (GC-14C, Shimadzu, Japan) with 300 W xenon lamp (PLS-SXE300/300UV, PerfectLight, Beijing, China) as light source. Photoelectrochemical detection was performed on an electrochemical workstation (CHI 618C, Chenhua Instrument, Shanghai, China). Transmission electron microscopy (TEM) was used for the morphology of the persistent photocatalysts at 200 kV (JEOL, JEM-2100, Japan). The crystal structure of nanoparticles was determined using a Bruker D8 Advance X-ray diffractometer (Germany) with a Cu-Kα radiation (λ = 1.5406 Å). X-ray photoelectron spectroscopy (XPS) and UPS of the samples were measured at X-ray photoelectron spectrometer (Escalab 250Xi, Thermo Fisher Scientific). The EPR spectra were recorded on an EPR spectrometer (JEOL, JES-FA 200, Japan). The UV-visible diffuse reflectance spectroscopy (UV-vis DRS) analysis was performed with a

UV-3600 spectrophotometer. Zeta potential for the samples was conducted using the Malvern Zetasizer Nano ZS system (Malvern, Zetasizer Nano ZS, UK). The interaction between the persistent photocatalyst and *R. palustris* was observed using a SEM (Zeiss Merlin Compact, Germany) and an energy-dispersive X-ray spectroscopy (EDS, Zeiss Merlin Compact, Germany) system. The viability of *R. palustris* was observed with a confocal laser scanning microscope (FV3000, OLYMPUS, Japan). Phosphorescence and excitation spectra of the materials, chlorophyll a, and *R. palustris* were collected with fluorescence spectrometer (Horiba, Fluorolog-QM, Kyoto, Japan) at room temperature. The absorbance spectra of chlorophyll a, *R. palustris*, and the co-culture system, before and after filtration, were measured using a UV-vis spectrophotometer (UV-2550, Shimadzu, Japan). The PL decay images of the samples were obtained using the IVIS Lumina XR imaging system (Caliper, USA). The concentration of lycopene was determined using a high-performance liquid chromatography (HPLC) system (Agilent Technologies, Palo Alto, CA, USA) equipped with a C18 reverse-phase column (4.6 × 250 mm). The content of ATP and NADP⁺/NADPH were determined by a microplate reader (BioTek Synergy H1, USA) based on the relative light units (RLUs) and optical density at 450 nm, respectively.

Synthesis of the persistent photocatalyst

The persistent photocatalyst was synthesized using a hydrothermal method. Briefly, Ga(NO₃)₃, Zn(NO₃)₂, Na₂GeO₃, and Ni(NO₃)₂ (optional) were sequentially added to a beaker according to the stoichiometric ratio. Subsequently, the pH of the precursor solution was adjusted to 8.5 with NH₃·H₂O (28 wt %) under magnetic stirring. After stirring at room temperature for 1 h, the solution was transferred into a Teflon-lined autoclave and reacted at 220 °C for 10 h. The resulting persistent photocatalyst of ZGGO or ZGGO:Ni was then obtained by centrifugation and washed with deionized water.

DFT calculations

The DFT within the Vienna ab-initio simulation package was applied to optimize the geometric structure of the persistent photocatalyst ZGGO:Ni. The interactions between ions and valence electrons were described using the projected-augmented wave method, while the exchange-related interaction of electrons was treated with the Perdew-Burke-Ernzerhof functional within the generalized gradient approximation. In the calculations presented in this work, the energy cutoff of 450 eV and gamma grid of 8 × 8 × 1 were set for model optimization and thermodynamics analyses. The atom positions were relaxed until the residual forces on each atom reached a convergence threshold of less than 0.02 eV/Å. The total energy was converged within an error of 1 × 10⁻⁵ eV for each atom. Spin polarization was allowed throughout the calculation. The (001) plane of ZGGO:Ni was used as the computational model. A vacuum space of 18 Å thickness in the z axis was used to avoid interactions between surface layers. The accurate band structure and DOS for the persistent photocatalyst were calculated by Heyd-Scuseria-Ernzerhof (HSE) hybrid functional theory. Additionally,

the charge transfer between different atoms was assessed by the Bader charge analysis method.

In principle, an ideal HER catalyst should hold a thermal-neutral (close to 0) Gibbs free energy of H atom adsorption ($\Delta G_H = 0$ eV). Under standard conditions, the HER pathway can be described as follows⁵⁹:



The Gibbs free energy of the adsorbed H atom (H^* H) on the catalyst is a key descriptor for the HER activity of the catalyst and is obtained as follows:

$$\Delta G_H = \Delta E_H + \Delta E_{ZPE} - T\Delta S.$$

Here, ΔE_H represents the adsorption energy; ΔE_{ZPE} represents the zero-point energy difference; T represents the temperature (298.15 K); and ΔS represents the entropy difference.

EPR of persistent photocatalyst

Oxygen vacancy defects in the persistent photocatalyst of ZGGO or ZGGO:Ni were investigated using an electron spin resonance spectrometer. The measuring parameters were set as follows: microwave power of 1 mW, microwave frequency of 9.20 GHz, magnetic field range of 305–355 mT, modulation width of 0.2 mT, scan time of 60 s, and test temperature of 113 K. Additionally, the influence of light on ZGGO:Ni was investigated by irradiating ZGGO:Ni with 300 W xenon lamp.

Photoelectrochemical measurements

The photocurrent properties and electrochemical impedance of the persistent photocatalyst were measured with a three-electrode system in an electrochemical workstation (CHI 618C, Chenhua, Shanghai, China). Ag/AgCl was used as the reference electrode, platinum foil as the counter electrode, fluorine-doped tin oxide (FTO) glass coated with the persistent photocatalyst as the working electrode, and 0.1 M Na₂SO₄ as the electrolyte. The photocurrent curves were recorded under the irradiation of a periodically switched 300 W xenon lamp.

Valence band energy calculation

The valence band energy (E_{VB}), which is equivalent to the ionization potential, was determined using UPS. Using the formula $h\nu + E_{Fermi} - E_{cutoff}$ (where $h\nu$ is 21.22 eV, representing the excitation energy of the He I Source Gun),⁶⁰ the E_{VB} of ZGGO and ZGGO:Ni were calculated to be 3.41 and 3.70 eV, respectively. According to the relationship between the vacuum energy ($E_{VB(vacuum)}$) and the normal hydrogen electrode (NHE) potential ($E_{VB(NHE)}$),⁶¹ the E_{VB} vs. NHE can be obtained as -7.91 and -8.20 V. Combined with the band gap from UV-vis diffuse reflectance spectra, the band position of ZGGO and ZGGO:Ni could be determined.

Band-gap calculation based on Tauc plot method

The band-gap energy of the persistent photocatalyst describes the energy required to excite an electron from the valence band to the conduction band. To determine the band gap of the persistent photocatalyst, the Tauc method was adopted,

as previous work reports.^{62,63} The Tauc method relies on the assumption that the energy-dependent absorption coefficient α can be expressed by the following equation,

$$(\alpha h\nu)^{\frac{1}{2}} = C(h\nu - E_g),$$

where h represents the Planck constant, ν represents the photo's frequency, E_g represents the band gap, and C is a constant. The γ factor depends on the nature of the electron transition and is equal to 1/2 or 2 for the direct and indirect transition band gaps, respectively. Here, the γ factor was set to 2 according to a previous reference.⁶⁴ According to the Tauc plot, the band gap of ZGGO and ZGGO:Ni were calculated to be 4.28 and 4.18 eV, respectively.

Decay images of persistent photocatalyst

50 mg of ZGGO:Ni persistent photocatalyst was placed in a 96-well plate and then exposed to a portable ultraviolet lamp for 2 min with an excitation wavelength of 254 nm. After the excitation ceased, the 96-well plate was immediately placed into the IVIS Lumina XR imaging system to record the PL decay images of the samples.

Hydrogen evolution test of the persistent photocatalyst

The photocatalytic hydrogen evolution was tested in a sealed reaction vessel (Pyrex glass) with a 300 W xenon lamp as the light source to simulate solar irradiation. Briefly, 50 mg of photocatalyst was suspended in a 50 mL aqueous solution containing 10 vol % TEOA as the sacrificial agent. The suspension was sonicated for 5 min, followed by thorough vacuum evacuation. The hydrogen produced by the photocatalyst was analyzed using a gas chromatograph.

Bacteria culture

R. palustris was cultured in Luria-Bertani (LB) medium that contains (per liter) 10 g peptone, 3 g beef extract, and 5 g NaCl. Considering that *R. palustris* was photosynthetic bacteria, a full-spectrum light-emitting diode (LED) lamp (100 W) was used as its light source. The *R. palustris* were cultured at 30°C with a shaking rate of 220 rpm. *Synechocystis* sp. PCC 6803 cells were grown in 200 mL BG11 medium. The cells were cultivated at 30°C, shaken at 220 rpm under constant illumination.

Interfacial interaction study of persistent photocatalyst/*R. palustris* biohybrids

The number of persistent photocatalyst nanoparticles that are in close physical interaction with *R. palustris* was determined via UV-vis absorption spectra.⁴² The rate constant of charge transfer at the persistent photocatalyst and *R. palustris* was calculated based on a physical model that considered the following kinetic processes⁴²: charge transfer between the persistent photocatalyst and *R. palustris* interface (k_{ET}), electron-hole recombination via non-radiative processes (k_{NR}), and electron-hole recombination via radiative processes (k_{PL}). According to the formulas below, the charge transfer between the persistent photocatalyst and *R. palustris* interface (k_{ET}) can be calculated.

$$\tau_{1(ZGGO:Ni)} = \frac{1}{k_{PL} + k_{NR}}$$

$$\tau_{1(ZGGO:Ni+R,p)} = \frac{1}{k_{PL} + k_{NR} + k_{ET}}$$

To obtain the rate constants, we further measured the decay curves of ZGGO:Ni and *R. palustris*-ZGGO:Ni, respectively. The decay curves were fitted with the following equation:

$$I(t) = A_1 e^{-\frac{t}{\tau_1}} + A_2 e^{-\frac{t}{\tau_2}}$$

Here $I(t)$ is intensity, and τ_1 and τ_2 are the decay times of the fast component and the slow component, respectively. Therefore, the electron transfer efficiency from the persistent photocatalyst to *R. palustris* in the co-culture system (ϕ_{ET}) can be further calculated with the following formula, which was calculated to be 86.37% in this work.

$$\phi_{ET} = \frac{k_{ET}}{k_{PL} + k_{NR} + k_{ET}}$$

Cell viability tests

Fluorescence images of *R. palustris* stained with PI and calcein acetoxymethyl ester (calcein AM) were measured using the confocal laser scanning microscope to test cell viability.

APCE calculations

The apparent photo conversion efficiency (APCE) values in this work were calculated following the method described by Li et al.⁴⁶ Specifically, APCE can be determined by the following formula:

$$APCE(\%) = \frac{E_B}{E_I}$$

$$E_B = v_B \times H_B \times V \times t$$

$$E_I = N_A \times I \times A \times t \times U$$

Here, E_B represents the energy fixed in biomass (J), and E_I represents the energy in actual incident light (J). v_B represents biomass growth rate ($\text{g L}^{-1} \text{day}^{-1}$); H_B represents the calorific value of biomass (J g^{-1}) assumed to be $6.03 \text{ kcal} \cdot \text{g}^{-1}$ ($25.23 \text{ kJ} \cdot \text{g}^{-1}$) based on a previous report.⁶⁵ V represents the working volume of the culture flask, which is 30 mL in this work. t represents culture time, 2 days. N_A represents Avogadro's constant ($6.022 \times 10^{23} \text{ mol}^{-1}$); I represents the actual incident light intensity, which was measured to be $76.82 \mu\text{mol m}^{-2} \text{ s}^{-1}$; A represents the cross-sectional area of the *R. palustris* suspension, measured to be 14.6 cm^2 ; U represents the average quantum energy of photos (J).

According to the above formulas, the APCE values are 4.10% for the control group (bare *R. palustris*) and 4.46% for *R. palustris* integrated with ZGGO:Ni.

NADPH generation with persistent photocatalyst *in vitro*

To investigate whether the persistent photocatalyst promotes the NADPH regeneration process, the reduction of NADP⁺ to NADPH was performed at room temperature. Specifically, [Cp^{*}Rh(bpy)H₂O]²⁺ (0.125 mM) was used as the electron shutter, TEOA (2 mM) as the sacrificial agent, and the photocatalyst (0.5 mg mL⁻¹) was added into NADP⁺ (1 mM) solution. Subsequently, the mixed solution was exposed to irradiation for 30 min using a portable UV lamp as the light source. After centrifugation, the regenerated NADPH was quantified by measuring its characteristic absorbance at 340 nm.

Determination of NADPH/NADP⁺ ratio and ATP concentration

R. palustris cultured under specified conditions was harvested. Subsequently, the ratio of NADP⁺/NADPH and ATP concentration in *R. palustris* were determined by NADP⁺/NADPH Assay Kit (WST-8) and Enhanced ATP Assay Kit, respectively. To be specific, *R. palustris* cells were treated with appropriate buffers as indicated by the providers. Subsequently, NADP⁺/NADPH ratios were detected using a colorimetric assay with a microplate reader at a detection wavelength of 450 nm, and ATP concentrations were determined by RLUs.

Determination of CO₂ fixation

To measure the CO₂ fixation rate, *R. palustris* and *Synechocystis*, with or without the addition of the persistent photocatalyst, were cultured under intermittent illumination by switching the light on and off every 12 h. For *R. palustris* culture, LB medium (10 g peptone, 3 g beef extract, and 5 g NaCl per liter) containing NaHCO₃ (30 mM) was adopted, and *R. palustris* was cultured at 30°C with a 100 W full-spectrum lamp as the light source. For *Synechocystis*, BG11 medium supplemented with 30 mM NaHCO₃ was adopted, and *Synechocystis* was cultured at 30°C with a 100 W full-spectrum lamp as the light source. The culture solution was then centrifuged at 8,000 rpm for 5 min to collect the supernatant. 98 wt % H₂SO₄ solution was diluted to a concentration of 5 mM for quantitative analysis of remaining HCO₃⁻ in the supernatant. The CO₂ fixation rate was calculated as: bicarbonate consumption (mM)/time interval (96 h)/DCW(g).

Lycopene extraction and titration

R. palustris was cultured with or without the addition of the persistent photocatalyst in an alternating 12-h light-dark cycle to imitate the intermittent nature of solar source. The bacterial cells were collected by centrifugation at 8,000 rpm for 5 min. The collected bacteria were then washed twice and resuspended with 1.0 g·L⁻¹ NaCl solution. After removing the supernatant by centrifugation, the obtained bacteria were dried at 70°C for 24 h. 3 mL of a 1:1 mixture of hexane and methanol was then added, and the mixture was shaken at 220 rpm for 30 min at room temperature in the dark to extract lycopene. After that, the mixture was centrifuged at 12,000 rpm for 10 min at 4°C to remove cell debris. The concentration of lycopene in the extract was determined with HPLC.

PHB extraction and titration

PHB was extracted and determined using the following methods. Specifically, 15 mL of *Synechocystis* cells (OD₇₃₀ approximately 1) were collected and centrifuged at 6,000 rpm for 10 min at 25°C. Then 1 mL concentrated H₂SO₄ was added and boiled for 1 h to hydrolyze PHB into crotonic acid.⁶⁶ The reaction solution was filtered through a 0.22 μm polytetrafluoroethylene membrane filter. Subsequently, 200 μL of the filtrate was diluted with 800 μL of 14 mM H₂SO₄ and subjected to an inert C18 column. The mobile phase consisted of 30% acetonitrile and 70% 10 mM KH₂PO₄ (pH 2.3) solution, with a flow rate of approximately 1.0 mL/min. Commercial crotonic acid was utilized as a detection reference.

Transcriptomics sequencing

Transcriptomics analysis has been conducted to comprehensively understand the functional mechanism of the persistent catalyst in *R. palustris*. Specifically, *R. palustris* was cultured with or without the addition of the persistent photocatalyst under intermittent illumination. After 4 days of culture, *R. palustris* samples were then collected. According to the manufacturer's instructions, total RNA was extracted from *R. palustris*, and its integrity was verified. The RNA was sent by Novogene to generate libraries. The RNA sequence reference data used in this study can be obtained from Taxonomy 1076 of the National Center for Biotechnology Information (NCBI) (<https://www.ncbi.nlm.nih.gov/Taxonomy/Browser/wwwtax.cgi?id=1076>).

Metabolomics analysis

According to the manufacturer's instructions, *R. palustris* samples cultured for 4 days were collected and sent by Novogene to generate libraries. The results obtained from mass spectrometry detection of the samples were analyzed using Compound Discoverer (v.3.3) for statistical analyses, including principal-component analysis (PCA), volcano plots, and heatmaps of differentially expressed microbial metabolites.

Shake-flask fermentation

Here, the culture of *R. palustris* is introduced as an example. The seeds of *R. palustris* were cultured in a 50 mL tube with a working volume of 30 mL. The O₂-free LB medium was used in the culture process. Subsequently, the obtained seed culture with the OD₆₀₀ approximately 0.8 was transferred into tubes containing 30 mL of LB medium and 30 mM NaHCO₃ at a volume ratio of 1%, either with or without the addition of the persistent photocatalyst. The fermentation temperature and agitation speed were set at 30°C and 220 rpm, respectively. Full-spectrum LED (100 W) was used for external lighting during the fermentation process to simulate the light-dark cycle of solar energy. In contrast, *Synechocystis* was cultured using O₂-free BG11 medium.

Fed-batch fermentation

Fed-batch fermentations were conducted in a 1.0 L fermenter with a working volume of 0.6 L. Similarly, the culture of *R. palustris* is introduced as an example. The *R. palustris* was cultured in O₂-free LB medium and transferred into a sterilized culture bottle with 400 mL O₂-free LB medium containing 30 mM NaHCO₃ when the culture reached an OD₆₀₀

approximately 0.8. Then the *R. palustris* seed was incubated at 30°C with an agitation speed of 220 rpm for 96 h, utilizing a full-spectrum LED (100 W) as its light source. Subsequently, 1% (v/v) seed culture was transferred into a sterilized fermenter, and the fed-batch fermentation started with feeding. An anaerobic condition inside the fermenter was established by flushing with argon gas until the concentration of dissolved oxygen reached zero. To maintain anaerobic conditions inside the fermenter, the feed medium (LB medium containing 30 mM NaHCO₃) was also flushed with argon gas before being fed into the fermenter. 3g/L HCl and 3g/L NaOH were used to control the pH of bacterial fermentation broth at ~7.0. Notably, *Synechocystis* was cultured using O₂-free BG11 medium.

LCA

LCA was conducted to analyze GHG emissions, economic cost, electricity consumption, and other comprehensive environmental impacts, according to the methodology standards described in ISO 14044. A “cradle to gate” system boundary was established with a functional unit of 1 kg of lycopene, excluding utility construction and end-of-life disposal.⁶⁷ Life-cycle inventories and emission factors for the bioproduction of 1 kg lycopene, with and without ZGGO:Ni in fermentation coupled with the downstream separation process, were calculated using the Ecoinvent database.^{68–70} A modified model of in-lab chemical synthesis of ZGGO:Ni, according to the lab data, along with the upstream industrial production of raw chemicals, was adopted here to comprehensively evaluate the environmental and economic impacts with less uncertainties.⁷¹ The production was considered to take place in southern China. GHG emissions equivalent and comprehensive environmental impact factors were obtained from the assessment using the IPCC-2021-GTP100 and ReCiPe-2016-Endpoint-(I) methods. Economic costs and electricity consumption were calculated based on the model.

Statistical analyses

All data are presented as mean ± standard deviation (SD), and statistical analyses and graphs were performed using OriginLab 9.0 and GraphPad Prism 8.0.1. For comparisons between two groups, significance was determined using two-tailed unpaired Student's *t* test.

RESOURCE AVAILABILITY

Lead contact

Further information and requests for resources should be directed to and will be fulfilled by the lead contact, Quan Yuan (yuanquan@whu.edu.cn).

Materials availability

All materials generated in this study are available from the [lead contact](#) without restriction.

Data and code availability

This study did not generate any datasets.

ACKNOWLEDGMENTS

This work is supported by the National Natural Science Foundation of China (21925401 and 52221001 to Q.Y.), the National Key R&D Program of China

(2023YFF1205900 to Q.Y.), the Fundamental Research Funds for the Central Universities (2042022rc0004 to Q.Y.), Hunan Provincial Key Research and Development Plan (2024JK2117 to Q.Y.), “Sharp Knife” Technology Research Program of Hubei Province (2023BAA002 to Q.Y.), China Postdoctoral Science Foundation (2024M752456 to N.C.), Postdoctoral Innovative Research of Hubei Province of China (211000025 to N.C.), Youth Talent Program of Sci-Tech Think Tank (XMSB20240710060 to N.C.), New Cornerstone Science Foundation through the XPLOER Prize, and Interdisciplinary Innovative Talents Foundation from Renmin Hospital of Wuhan University. We thank the Core Facility of Wuhan University for SEM and TEM analysis.

AUTHOR CONTRIBUTIONS

Conceptualization: Q.Y., L.Y., Y.Z., and N.C.; methodology: N.C., J.X., T.H., R.S., R.Z., H.C., J.Y., and N.D.; investigation: N.C., J.X., and T.H.; visualization: T.H. and R.S.; supervision: Q.Y., Y.Z., L.Y., and N.C.; writing—original draft: N.C.; writing—review and editing: Q.Y., T.L., Y.Z., L.Y., and T.P.

DECLARATION OF INTERESTS

The authors declare no competing interests.

SUPPLEMENTAL INFORMATION

Supplemental information can be found online at <https://doi.org/10.1016/j.chempr.2024.11.019>.

Received: June 22, 2024

Revised: October 14, 2024

Accepted: November 19, 2024

Published: January 3, 2025

REFERENCES

- Dogutan, D.K., and Nocera, D.G. (2019). Artificial photosynthesis at efficiencies greatly exceeding that of natural photosynthesis. *Acc. Chem. Res.* 52, 3143–3148. <https://doi.org/10.1021/acs.accounts.9b00380>.
- Sakimoto, K.K., Wong, A.B., and Yang, P. (2016). Self-photosensitization of nonphotosynthetic bacteria for solar-to-chemical production. *Science* 351, 74–77. <https://doi.org/10.1126/science.aad3317>.
- Li, C., Liu, J., Li, H., Wu, K., Wang, J., and Yang, Q. (2022). Covalent organic frameworks with high quantum efficiency in sacrificial photocatalytic hydrogen evolution. *Nat. Commun.* 13, 2357. <https://doi.org/10.1038/s41467-022-30035-x>.
- Lv, J., Xie, J., Mohamed, A.G.A., Zhang, X., Feng, Y., Jiao, L., Zhou, E., Yuan, D., and Wang, Y. (2023). Solar utilization beyond photosynthesis. *Nat. Rev. Chem.* 7, 91–105. <https://doi.org/10.1038/s41570-022-00448-9>.
- Kosco, J., Gonzalez-Carrero, S., Howells, C.T., Fei, T., Dong, Y., Sougrat, R., Harrison, G.T., Firdaus, Y., Sheelamanthula, R., Purushothaman, B., et al. (2022). Generation of long-lived charges in organic semiconductor heterojunction nanoparticles for efficient photocatalytic hydrogen evolution. *Nat. Energy* 7, 340–351.
- Li, C., Wang, R., Wang, J., Liu, L., Li, H., Zheng, H., and Ni, J. (2023). A highly compatible phototrophic community for carbon-negative biosynthesis. *Angew. Chem. Int. Ed. Engl.* 62, e202215013. <https://doi.org/10.1002/anie.202215013>.
- Hu, G., Li, Z., Ma, D., Ye, C., Zhang, L., Gao, C., Liu, L., and Chen, X. (2021). Light-driven biosynthesis of volatile, unstable and photosensitive chemicals from CO₂. *Nat. Catal.* 4, 960–971.
- Li, C., Yin, L., Wang, J., Zheng, H., and Ni, J. (2023). Light-driven biosynthesis of volatile, unstable and photosensitive chemicals from CO₂. *Nat. Synth.* 2, 960–971.
- Chen, W.J., Yu, W., Wang, Z.H., Gao, Z.Q., Zhang, M.M., Zhu, C.W., Lv, F.T., Huang, Y.M., Bai, H.T., and Wang, S. (2023). Self-powered biohybrid

- systems based on organic materials for sustainable biosynthesis. *ACS Appl. Mater. Interfaces* **16**, 19914–19925. <https://doi.org/10.1021/ac-sami.3c12400>.
- Chen, W.J., Lin, H.R., Yu, W., Huang, Y.M., Lv, F.T., Bai, H.T., and Wang, S. (2024). Organic semiconducting polymers for augmenting biosynthesis and bioconversion. *JACS Au* **4**, 3–19. <https://doi.org/10.1021/jacsau.3c00576>.
 - Ni, J., Liu, H.-Y., Tao, F., Wu, Y.-T., and Xu, P. (2018). Remodeling of the photosynthetic chain promotes direct CO₂ conversion into valuable aromatic compounds. *Angew. Chem. Int. Ed. Engl.* **57**, 15990–15994. <https://doi.org/10.1002/anie.201808402>.
 - Wang, B., and Dai, Z. (2023). Engineering photosynthetic microbial consortia for carbon-negative biosynthesis. *Angew. Chem. Int. Ed. Engl.* **62**, e202217961. <https://doi.org/10.1002/anie.202217961>.
 - Loh, J.Y.Y., Kherani, N.P., and Ozin, G.A. (2021). Persistent CO₂ photocatalysis for solar fuels in the dark. *Nat. Sustain.* **4**, 466–473.
 - Miller, T.E., Beneyton, T., Schwander, T., Diehl, C., Girault, M., McLean, R., Chotel, T., Claus, P., Cortina, N.S., Baret, J.-C., et al. (2020). Light-powered CO₂ fixation in a chloroplast mimic with natural and synthetic parts. *Science* **368**, 649–654. <https://doi.org/10.1126/science.aaz6802>.
 - Wang, J., Chen, N., Bian, G., Mu, X., Du, N., Wang, W., Ma, C.-G., Fu, S., Huang, B., Liu, T., et al. (2022). Solar-driven overproduction of biofuels in microorganisms. *Angew. Chem. Int. Ed. Engl.* **61**, e202207132. <https://doi.org/10.1002/anie.202207132>.
 - Zhou, J., Zhang, F., Meng, H., Zhang, Y., and Li, Y. (2016). Introducing extra nadph consumption ability significantly increases the photosynthetic efficiency and biomass production of cyanobacteria. *Metab. Eng.* **38**, 217–227. <https://doi.org/10.1016/j.ymben.2016.08.002>.
 - Sun, T., Li, Z., Li, S., Chen, L., and Zhang, W. (2023). Exploring and validating key factors limiting cyanobacteria-based CO₂ bioconversion: Case study to maximize myo-inositol biosynthesis. *Chem. Eng. J.* **452**, 139158.
 - Cui, G., Yang, X., Zhang, Y., Fan, Y., Chen, P., Cui, H., Liu, Y., Shi, X., Shang, Q., and Tang, B. (2019). Round-the-clock photocatalytic hydrogen production with high efficiency by a long-afterglow material. *Angew. Chem. Int. Ed. Engl.* **58**, 1340–1344. <https://doi.org/10.1002/anie.201810544>.
 - Cai, T., Liu, Y., Wang, L., Dong, W., and Zeng, G. (2019). Recent advances in round-the-clock photocatalytic system: Mechanisms, characterization techniques and applications. *J. Photochem. Photobiol. C* **39**, 58–75.
 - Fang, X., Kalathil, S., and Reisner, E. (2020). Semi-biological approaches to solar-to-chemical conversion. *Chem. Soc. Rev.* **49**, 4926–4952. <https://doi.org/10.1039/c9cs00496c>.
 - Shi, X., Huang, Y., Long, R., Wang, Z., Wang, L., Cao, J., Zhu, G., and Xiong, Y. (2024). Sustainable all-weather CO₂ utilization by mimicking natural photosynthesis in a single material. *Natl. Sci. Rev.* **11**, nwad275. <https://doi.org/10.1093/nsr/nwad275>.
 - Liu, C., Colón, B.C., Ziesack, M., Silver, P.A., and Nocera, D.G. (2016). Water splitting-biosynthetic system with CO₂ reduction efficiencies exceeding photosynthesis. *Science* **352**, 1210–1213. <https://doi.org/10.1126/science.aaf5039>.
 - Wang, Q., Kalathil, S., Pornrunroj, C., Sahm, C.D., and Reisner, E. (2022). Bacteria-photocatalyst sheet for sustainable carbon dioxide utilization. *Nat. Catal.* **5**, 746.
 - Ostwald, W. (1907). The modern theory of energetics. *Monist* **17**, 481–515.
 - Rodrigues, R.M., Guan, X., Iniguez, J.A., Estabrook, D.A., Chapman, J.O., Huang, S., Sletten, E.M., and Liu, C. (2019). Perfluorocarbon nanoemulsion promotes the delivery of reducing equivalents for electricity-driven microbial CO₂ reduction. *Nat. Catal.* **2**, 407–414.
 - Zhang, Y., Zhang, Y., Zhang, H., Bai, L., Hao, L., Ma, T., and Huang, H. (2021). Defect engineering in metal sulfides for energy conversion and storage. *Coord. Chem. Rev.* **448**, 214147.
 - Schulz, M., Hagmeyer, N., Wehmeyer, F., Lowe, G., Rosenkranz, M., Seidler, B., Popov, A., Streb, C., Vos, J.G., and Dietzek, B. (2020). Photoinduced charge accumulation and prolonged multielectron storage for the separation of light and dark reaction. *J. Am. Chem. Soc.* **142**, 15722–15728. <https://doi.org/10.1021/jacs.0c03779>.
 - Liu, L.-L., Chen, F., Wu, J.-H., Ke, M.-K., Cui, C., Chen, J.-J., and Yu, H.-Q. (2022). Edge electronic vacancy on ultrathin carbon nitride nanosheets anchoring O₂ to boost H₂O₂ photoproduction. *Appl. Catal. B* **302**, 120845.
 - Xiao, Y., Feng, C., Fu, J., Wang, F., Li, C., Kunzelmann, V.F., Jiang, C.-M., Nakabayashi, M., Shibata, N., Sharp, I.D., et al. (2020). Band structure engineering and defect control of Ta₃N₅ for efficient photoelectrochemical water oxidation. *Nat. Catal.* **3**, 932–940.
 - Pei, L., Ma, Z., Zhong, J., Li, W., Wen, X., Guo, J., Liu, P., Zhang, Z., Mao, Q., Zhang, J., et al. (2022). Oxygen vacancy-rich Sr₂MgSi₂O₇:Eu²⁺, Dy³⁺-long afterglow phosphor as a round-the-clock catalyst for selective reduction of CO₂ to CO. *Adv. Funct. Mater.* **32**, 2208565.
 - Bo, Y., Wang, H., Lin, Y., Yang, T., Ye, R., Li, Y., Hu, C., Du, P., Hu, Y., Liu, Z., et al. (2021). Altering hydrogenation pathways in photocatalytic nitrogen fixation by tuning local electronic structure of oxygen vacancy with dopant. *Angew. Chem. Int. Ed. Engl.* **60**, 16085–16092. <https://doi.org/10.1002/anie.202104001>.
 - Xu, X., Ren, J., Chen, G., Kong, D., Gu, C., Chen, C., and Kong, L. (2013). Bright green emission from the Mn²⁺-doped zinc gallogermanate phosphors. *Opt. Mater. Express* **3**, 1727–1732.
 - Zhang, Y., Tao, L., Xie, C., Wang, D., Zou, Y., Chen, R., Wang, Y., Jia, C., and Wang, S. (2020). Defect engineering on electrode materials for rechargeable batteries. *Adv. Mater.* **32**, e1905923. <https://doi.org/10.1002/adma.201905923>.
 - Ruan, Q., Xi, X., Yan, B., Kong, L., Jiang, C., Tang, J., and Sun, Z. (2023). Stored photoelectrons in a faradaic junction for decoupled solar hydrogen production in the dark. *Chem* **9**, 1850–1864.
 - Ou, X., Qin, X., Huang, B., Zan, J., Wu, Q., Hong, Z., Xie, L., Bian, H., Yi, Z., Chen, X., et al. (2021). High-resolution x-ray luminescence extension imaging. *Nature* **590**, 410–415. <https://doi.org/10.1038/s41586-021-03251-6>.
 - Liang, L., Chen, J., Shao, K., Qin, X., Pan, Z., and Liu, X. (2023). Controlling persistent luminescence in nanocrystalline phosphors. *Nat. Mater.* **22**, 289–304. <https://doi.org/10.1038/s41563-022-01468-y>.
 - Pei, P., Chen, Y., Sun, C., Fan, Y., Yang, Y., Liu, X., Lu, L., Zhao, M., Zhang, H., Zhao, D., et al. (2021). X-ray-activated persistent luminescence nanomaterials for NIR-II imaging. *Nat. Nanotechnol.* **16**, 1011–1018. <https://doi.org/10.1038/s41565-021-00922-3>.
 - Liang, L., Chen, N., Jia, Y., Ma, Q., Wang, J., Yuan, Q., and Tan, W. (2019). Recent progress in engineering near-infrared persistent luminescence nanoprobes for time-resolved biosensing/bioimaging. *Nano Res.* **12**, 1279–1292.
 - Lubitz, W., Ogata, H., Rüdiger, O., and Reijerse, E. (2014). Hydrogenases. *Chem. Rev.* **114**, 4081–4148. <https://doi.org/10.1021/cr4005814>.
 - Kim, J., Jang, J., Hilberath, T., Hollmann, F., and Park, C.B. (2022). Photoelectrocatalytic biosynthesis fuelled by microplastics. *Nat. Sustain.* **1**, 776–786.
 - Yu, W., Zeng, Y., Wang, Z., Xia, S., Yang, Z., Chen, W., Huang, Y., Lv, F., Bai, H., and Wang, S. (2023). Solar-powered multi-organism symbiotic mimic system for beyond natural synthesis of polypeptides from CO₂ and N₂. *Sci. Adv.* **9**, ead6772. <https://doi.org/10.1126/sciadv.ad6772>.
 - Guan, X., Erşan, S., Hu, X., Atallah, T.L., Xie, Y., Lu, S., Cao, B., Sun, J., Wu, K., Huang, Y., et al. (2022). Maximizing light-driven CO₂ and N₂ fixation efficiency in quantum dot-bacteria hybrids. *Nat. Catal.* **5**, 1019–1029. <https://doi.org/10.1038/s41929-022-00867-3>.
 - Sahoo, P.C., Pant, D., Kumar, M., Puri, S.K., and Ramakumar, S.S.V. (2020). Material-microbe interfaces for solar-driven CO₂

- bioelectrosynthesis. *Trends Biotechnol.* **38**, 1245–1261. <https://doi.org/10.1016/j.tibtech.2020.03.008>.
44. Zhang, H., Liu, H., Tian, Z., Lu, D., Yu, Y., Cestellos-Blanco, S., Sakimoto, K.K., and Yang, P. (2018). Bacteria photosensitized by intracellular gold nanoclusters for solar fuel production. *Nat. Nanotechnol.* **13**, 900–905. <https://doi.org/10.1038/s41565-018-0267-z>.
 45. Yu, Y.-Y., Wang, Y.-Z., Fang, Z., Shi, Y.-T., Cheng, Q.-W., Chen, Y.-X., Shi, W., and Yong, Y.-C. (2020). Single cell electron collectors for highly efficient wiring-up electronic abiotic/biotic interfaces. *Nat. Commun.* **11**, 4087. <https://doi.org/10.1038/s41467-020-17897-9>.
 46. Li, D., Dong, H., Cao, X., Wang, W., and Li, C. (2023). Enhancing photosynthetic CO₂ fixation by assembling metal-organic frameworks on chlorella pyrenoidosa. *Nat. Commun.* **14**, 5337. <https://doi.org/10.1038/s41467-023-40839-0>.
 47. Chen, N., Du, N., Shen, R., He, T., Xi, J., Tan, J., Bian, G., Yang, Y., Liu, T., Tan, W., et al. (2023). Redox signaling-driven modulation of microbial biosynthesis and biocatalysis. *Nat. Commun.* **14**, 6800. <https://doi.org/10.1038/s41467-023-42561-3>.
 48. Chen, N., Du, N., Wang, W., Liu, T., Yuan, Q., and Yang, Y. (2022). Real-time monitoring of dynamic microbial Fe(III) respiration metabolism with a living cell-compatible electron-sensing probe. *Angew. Chem. Int. Ed. Engl.* **61**, e202115572. <https://doi.org/10.1002/anie.202115572>.
 49. Guzman, M.S., Rengasamy, K., Binkley, M.M., Jones, C., Ranaivoarisoa, T.O., Singh, R., Fike, D.A., Meacham, J.M., and Bose, A. (2019). Phototrophic extracellular electron uptake is linked to carbon dioxide fixation in the bacterium *rhodospseudomonas palustris*. *Nat. Commun.* **10**, 1355. <https://doi.org/10.1038/s41467-019-09377-6>.
 50. Cui, R.Y., Hultman, N., Edwards, M.R., He, L., Sen, A., Surana, K., McJeon, H., Iyer, G., Patel, P., Yu, S., et al. (2019). Quantifying operational lifetimes for coal power plants under the paris goals. *Nat. Commun.* **10**, 4759. <https://doi.org/10.1038/s41467-019-12618-3>.
 51. Peng, W., Wagner, F., Ramana, M.V., Zhai, H., Small, M.J., Dalin, C., Zhang, X., and Mauzerall, D.L. (2018). Managing China's coal power plants to address multiple environmental objectives. *Nat. Sustain.* **1**, 693–701.
 52. Xing, X., Wang, R., Bauer, N., Ciaias, P., Cao, J., Chen, J., Tang, X., Wang, L., Yang, X., Boucher, O., et al. (2021). Spatially explicit analysis identifies significant potential for bioenergy with carbon capture and storage in china. *Nat. Commun.* **12**, 3159. <https://doi.org/10.1038/s41467-021-23282-x>.
 53. Martins, V.F.D., Miguel, C.V., Goncalves, J.C., Rodrigues, A.E., and Madeira, L.M. (2022). Modeling of a cyclic sorption-desorption unit for continuous high temperature CO₂ capture from flue gas. *Chem. Eng. J.* **434**, 134704.
 54. Christie-Oleza, J.A., Sousoni, D., Lloyd, M., Armengaud, J., and Scanlan, D.J. (2017). Nutrient recycling facilitates long-term stability of marine microbial phototroph-heterotroph interactions. *Nat. Microbiol.* **2**, 17100. <https://doi.org/10.1038/nmicrobiol.2017.100>.
 55. Hutchins, D.A., and Fu, F. (2017). Microorganisms and ocean global change. *Nat. Microbiol.* **2**, 17058. <https://doi.org/10.1038/nmicrobiol.2017.58>.
 56. Jansson, J.K. (2023). Microorganisms, climate change, and the sustainable development goals: Progress and challenges. *Nat. Rev. Microbiol.* **21**, 622–623. <https://doi.org/10.1038/s41579-023-00953-8>.
 57. Chen, X., Lawrence, J.M., Wey, L.T., Schertel, L., Jing, Q., Vignolini, S., Howe, C.J., Kar-Narayan, S., and Zhang, J.Z. (2022). 3D-printed hierarchical pillar array electrodes for high-performance semi-artificial photosynthesis. *Nat. Mater.* **21**, 811–818. <https://doi.org/10.1038/s41563-022-01205-5>.
 58. Sleutel, T., Sebastião Bernardo, R.S., Kuntke, P., Janssen, M., Buisman, C.J.N., and Hamelers, H.V.M. (2020). Enhanced phototrophic biomass productivity through supply of hydrogen gas. *Environ. Sci. Technol. Lett.* **7**, 861–865. <https://doi.org/10.1021/acs.estlett.0c00718>.
 59. Wang, D., Liu, X., Kang, Y., Wang, X., Wu, Y., Fang, S., Yu, H., Memon, M.H., Zhang, H., Hu, W., et al. (2021). Bidirectional photocurrent in p-n heterojunction nanowires. *Nat. Electron.* **4**, 645–652.
 60. Zhao, D., Wang, Y., Dong, C.-L., Huang, Y.-C., Chen, J., Xue, F., Shen, S., and Guo, L. (2021). Boron-doped nitrogen-deficient carbon nitride-based z-scheme heterostructures for photocatalytic overall water splitting. *Nat. Energy* **6**, 388–397.
 61. Li, N., Than, A., Sun, C., Tian, J., Chen, J., Pu, K., Dong, X., and Chen, P. (2016). Monitoring dynamic cellular redox homeostasis using fluorescence-switchable graphene quantum dots. *ACS Nano* **10**, 11475–11482. <https://doi.org/10.1021/acs.nano.6b07237>.
 62. Makula, P., Pacia, M., and Macyk, W. (2018). How to correctly determine the band gap energy of modified semiconductor photocatalysts based on UV-Vis spectra. *J. Phys. Chem. Lett.* **9**, 6814–6817. <https://doi.org/10.1021/acs.jpcclett.8b02892>.
 63. Liu, F., Shi, R., Wang, Z., Weng, Y., Che, C.-M., and Chen, Y. (2019). Direct z-scheme hetero-phase junction of black/red phosphorus for photocatalytic water splitting. *Angew. Chem. Int. Ed. Engl.* **58**, 11791–11795. <https://doi.org/10.1002/anie.201906416>.
 64. Oshima, T., Niwa, M., Mukai, A., Nagami, T., Suyama, T., and Ohtomo, A. (2014). Epitaxial growth of wide-band-gap ZnGa₂O₄ films by mist chemical vapor deposition. *J. Cryst. Growth* **386**, 190–193.
 65. Carozzi, P., and Sacchi, A. (2001). Biomass production and studies on *rhodospseudomonas palustris* grown in an outdoor, temperature controlled, underwater tubular photobioreactor. *J. Biotechnol.* **88**, 239–249. [https://doi.org/10.1016/s0168-1656\(01\)00280-2](https://doi.org/10.1016/s0168-1656(01)00280-2).
 66. Rueda, E., Álvarez-González, A., Vila, J., Díez-Montero, R., Grifoll, M., and García, J. (2022). Inorganic carbon stimulates the metabolic routes related to the polyhydroxybutyrate production in a *synechocystis* sp. Strain (cyanobacteria) isolated from wastewater. *Sci. Total Environ.* **829**, 154691. <https://doi.org/10.1016/j.scitotenv.2022.154691>.
 67. Pi, A.S., Yang, W.J., Feng, W., Yang, R.J., Chao, W.X., Cheng, W.B., Cui, L., Li, Z.D., Lin, Y.L., Ren, N.Q., et al. (2023). Solar-driven waste-to-chemical conversion by wastewater-derived semiconductor biohybrids. *Nat. Sustain.* **6**, 1673–1684.
 68. Balgobin, T., Brandam, C., and Joannis-Cassan, C. (2024). Influence of process parameters on the environmental impact of 2,3-buta-nediol production by fermentation. *Biochem. Eng. J.* **209**, 109374.
 69. Bippus, L., Briem, A.K., Beck, A., Zibek, S., and Albrecht, S. (2024). Life cycle assessment for early-stage process optimization of microbial biosurfactant production using kinetic models—a case study on mannosylerythritol lipids (MEL). *Front. Bioeng. Biotechnol.* **12**, 1347452. <https://doi.org/10.3389/fbioe.2024.1347452>.
 70. Lu, Y., Mu, D.Y., Xue, Z.L., Xu, P.L., Li, Y.M., Xiang, W.L., Burnett, J., Bryant, K., and Zhou, W.G. (2021). Life cycle assessment of industrial production of microalgal oil from heterotrophic fermentation. *Algal Res.* **58**, 102404.
 71. Nan, T.X., Yang, J.G., Aromaa-Stubb, R., Zhu, Q., He, H.B., and Lundstrom, M. (2024). Extracting valuable metals from zinc sulfide concentrate: A comprehensive simulation-based life cycle assessment study of oxidative pressure leaching. *Miner. Eng.* **276**, 108888.